

Stability analysis of BWR nuclear-coupled thermal-hydraulics using a simple model¹

Atul A. Karve^{a,*}, Rizwan uddin^{b,2}, J.J. Dorning^{a,c}

^a *Department of Mechanical, Aerospace and Nuclear Engineering, University of Virginia, Charlottesville, VA 22903, USA*

^b *Department of Nuclear Engineering and Computational Science & Engineering, University of Illinois, 214 NEL, 103 South Goodwin Avenue, Urbana, IL 61801, USA*

^c *Department of Applied Mathematics, University of Virginia, Charlottesville, VA 22903, USA*

Abstract

A simple mathematical model is developed to describe the dynamics of the nuclear-coupled thermal-hydraulics in a boiling water reactor (BWR) core. The model, which incorporates the essential features of neutron kinetics and single-phase and two-phase thermal-hydraulics, leads to a simple dynamical system comprised of a set of nonlinear ordinary differential equations (ODEs). The stability boundary is determined and plotted in the inlet-subcooling-number (enthalpy)/external-reactivity operating parameter plane. The eigenvalues of the Jacobian matrix of the dynamical system also are calculated at various steady-states (fixed points); the results are consistent with those of the direct stability analysis and indicate that a Hopf bifurcation occurs as the stability boundary in the operating parameter plane is crossed. Numerical simulations of the time-dependent, nonlinear ODEs are carried out for selected points in the operating parameter plane to obtain the actual damped and growing oscillations in the neutron number density, the channel inlet flow velocity, and the other phase variables. These indicate that the Hopf bifurcation is subcritical, hence, density wave oscillations with growing amplitude could result from a finite perturbation of the system even when it is being operated in the parameter region thought to be safe, i.e. where the steady-state is stable. Finally, the power-flow map, frequently used by reactor operators during start-up and shut-down operation of a BWR, is mapped to the inlet-subcooling-number/neutron-density (operating-parameter/phase-variable) plane, and then related to the stability boundaries for different fixed inlet velocities corresponding to selected points on the flow-control line. Also, the stability boundaries for different fixed inlet subcooling numbers corresponding to those selected points, are plotted in the neutron-density/inlet-velocity phase variable plane and then the points on the flow-control line are related to their respective stability boundaries in this plane. The relationship of the operating points on the flow-control line to their respective stability boundaries in these two planes provides insight into the instability observed in BWRs during low-flow/high-power operating conditions. It also shows that the normal operating point of a BWR is very stable in comparison with other possible operating points on the power-flow map. © 1997 Elsevier Science S.A.

* Corresponding author. Tel.: +1 804 9825473; e-mail: aak5s@virginia.edu

¹ This research was supported in part by the US NRC under grant No. NRC-04-90-113 and in part by the US DOE under grant No. DE-FG05-92ER75788. The opinions, findings, conclusions, and recommendations expressed herein are those of the authors and do not necessarily reflect the views of the NRC or DOE.

² Work performed while at the University of Virginia.

1. Introduction

Following several incidents of density-wave oscillations (DWOs) during operational transients in boiling reactor cores (BWR), the study of this instability from an operational and a safety point of view, has become very relevant and important. Over the past several years, many mathematical models and computational codes have been developed, and tests have been carried out to investigate this problem. In the work carried out so far, stability analyses usually have been carried out by evaluating the decay ratios and studying the effect of certain parameters on BWR stability. Numerical simulations have been done to study the time evolution of certain phase variables. The results of some of these stability analyses and numerical simulations have been compared with test results or data collected from actual BWR instability incidents and the overall agreement has been reasonably good. However, in the various models and codes developed, either no attempt has been made to determine the stability boundary in an operating parameter plane, or the models and codes are mathematically and computationally so complex that only a few points approximating the stability boundary are computed. It has thus been the purpose of the research reported here to develop a model that is simple and yet retains the essential physical dynamics of BWR thermal-hydraulics and neutron kinetics and therefore can be used both to carry out extensive stability analyses and to provide a starting point for a more complete, yet simple, model for the nonlinear dynamics of a BWR.

Belblidia et al. (1983) carried out a nodal analysis of DWOs in BWRs. They showed that the point kinetics model representation of the BWR neutronics yields conservative results, although for better assessment of BWR core stability radial coupling effects should be included. The mass-flux/pressure-drop results predicted by their model compared well with production codes such as FIBWR and COBRA-III. Peng et al. (1984) developed a linear frequency domain computer code NUFREQ-NP for BWR stability analysis under conditions of either forced or natural circulation. That code is based on a one-dimensional drift flux model for the two-phase flow and takes into account subcooled

boiling, arbitrary nonuniform axial and radial power shapes, distributed local losses, detailed fuel element dynamics and system pressure perturbation. Peng et al. (1984) compared stability results they obtained using it with experimental data from Peach Bottom-2 stability tests and found good agreement. March-Leuba et al. (1986a) developed a phenomenological model to simulate the 'qualitative' behavior of BWRs. They also developed a detailed nodalized (numerically discretized) physical model to simulate the dynamic behavior of the Vermont Yankee BWR over a broad operating range by varying the power and flow (March-Leuba et al., 1986b). Their analysis led to the conclusion that for a wide range of oscillation amplitudes, no significant effect on the integrity of the fuel is expected. However, in order to keep their model simple, they assumed that the coolant enters the core at saturation enthalpy (not as a subcooled liquid), i.e. that the boiling boundary always is at the bottom of the core channels. Valtonen (1989) validated the RAMONA-3B and TRAB BWR transient codes using DWO data from an oscillation incident that occurred at the TVO-1 BWR. It was shown that both spatially out-of-phase and spatially in-phase oscillations are possible in BWRs and that decreasing the fuel gas gap conductance has a destabilizing effect. Bergdahl et al. (1989) investigated the BWR stability at Forsmark-1 and showed that the decay ratio ranged considerably higher than that expected based on code calculations. Rizwan-uddin and Dorning (1992) studied the effects of unheated riser sections that are added to enhance natural circulation in advanced and simple BWRs. They found that, for a fixed flow rate, the addition of the riser sections makes the system less stable. They also showed that the feedback recirculation loop plays an important role in reactor stability and if omitted from the model, can lead to nonconservative conclusions. Wulff et al. (1992) simulated the instability that occurred at the LaSalle-2 power plant (and several other BWR transients) using the Brookhaven National Laboratory Engineering Plant Analyzer (EPA) in order to determine the causes that lead to the observed magnitudes of power, flow and temperature oscillations. They found it to be a powerful tool for scoping calculations and for supporting accident

management. Although very valuable in many contexts, production codes such as EPA are not very useful for thorough stability analyses or extensive parameter studies in general, because of their complexity and large computer running times. Ward and Lee (1987) developed a simplified BWR core model—where they described the neutronics by the point kinetics equation without any delayed precursor group, had a single node representation of the fuel rod temperature dynamics, and simplified the thermal hydraulics representation of the two phases in the flow channel by omitting the temporal acceleration term in the momentum equations—and by singular perturbation analysis, presented extensive results on limit-cycle behavior in neutronics-coupled DWOs. While all the works cited above on stability analysis of BWRs were performed either using a time-domain (nonlinear, numerical) approach or a frequency-domain (linear) approach, Tsuji et al. (1993) developed a simple BWR core model as a dynamical system comprised of a set of nonlinear ODEs and used bifurcation theory to investigate the dependencies of the fixed point (steady-state) on the parameters—such as the inlet pressure loss coefficient, the inlet subcooling, the gap conductivity between the fuel and cladding, the system pressure and the void reactivity feedback coefficient—which have a large influence on the stability of BWRs. They also showed that loss of stability took place at low-flow/high-power conditions and that sustained limit-cycle in-phase power oscillations observed in BWR instabilities were not directly excited by the subcritical Hopf bifurcation that resulted from their model.

Accurate models for the study of the stability of boiling flow without nuclear coupling also have been developed. Achard et al. (1985) developed one, starting from the homogeneous equilibrium model for the two-phase flow, which led to two functional differential equations (FDEs) with complicated nonlinear delay multiple integral operators. Rizwan-uddin and Dorning (1986) extended that model by starting from the drift-flux equations to represent the two-phase flow and not surprisingly arrived at considerably more complicated FDEs, which they analyzed. However, by starting from the homogeneous equilibrium model and

introducing some simplifying assumptions, Clause and Lahey (1991) developed a simple model for the boiling flow problem that yields a rich variety of nonlinear phenomena, many of which are similar to those that result from the much more complicated FDE models (Achard et al., 1985; Rizwan-uddin and Dorning, 1986) and also are similar to those observed experimentally.

Following Clause and Lahey (1991) and motivated by the desire to represent a BWR as a simple dynamical system, we have extended their model by including neutron kinetics and heat conduction in the fuel rods to develop a basic model for the dynamics of BWR along the lines of those developed in Ward and Lee (1987) and Tsuji et al. (1993) and we have used it to carry out stability analyses and to do numerical simulations. This model is simple in that the dynamical system that results is comprised of a set of nonlinear ODEs rather than complicated FDEs, yet it incorporates the essential features of neutron kinetics, fuel rod dynamics and single- and two-phase flow thermal-hydraulics. Most previous ODE-based models developed to represent BWR dynamics (such as those reported in March-Leuba et al. (1986a) and Tsuji et al. (1993)) are based on approaches in which the phase variables are discretized via finite-difference approximations, or by ‘nodalization’ procedures in which they are discretized along vertical segments of the coolant channel length by approximating them as spatially constant (but time-dependent) within these segments or nodes. Rather, we follow the weighted-residual-like approach introduced by Clause and Lahey (1991) in their simple linear approximations of the space dependence of the enthalpies in the single-phase region and the two-phase region. These approximations lead to three ODEs for the single- and two-phase flow, which are combined here with the ODEs of point neutron kinetics and the ODEs of heat conduction in the fuel rod obtained by reducing the heat conduction PDE to ODEs using two approaches—a simple eigenfunction expansion method and a variational method. The resulting set of ODEs can be analyzed straightforwardly using standard techniques of bifurcation theory to determine the DWO stability boundaries in various parameter planes. This was done and the results are presented in the most relevant parameter plane—the inlet-sub-

cooling-number (enthalpy)/external-reactivity operating parameter plane. Although the mass flow rate (proportional to the core inlet velocity) and the power (proportional to the neutron density) are phase variables (unknowns) and not parameters of the dynamical system, they are the coordinates of the power-flow map used during start-up and shut-down operations of a BWR and the mass flow rate actually is used as the practical control variable during these operations. Thus, it is useful to relate operating points on a typical BWR power-flow map to the stability boundaries in operating-parameter/phase-variable planes. Hence, the stability boundaries are also calculated and presented in the inlet-subcooling-number/neutron-density (operating-parameter/phase-variable) plane and the neutron-density/inlet-velocity phase variable plane. Selected points on the flow-control line are then related to their respective stability boundaries in these two planes to qualitatively explain the instabilities observed during operation of BWRs at low-flow/high-power operating conditions and also to show that the normal operating point of a BWR is very stable in comparison with other possible operating points on the power-flow map. Direct numerical integration of the set of nonlinear ODEs are consistent with the results of the stability analysis, and further indicate the nature of the bifurcation.

2. Description of the model

In this section we first describe the physical model developed and employed, and then present the dynamical system that results, i.e. the set of final nonlinear ODEs. Details of the model development procedure are given in the following section. A BWR lattice cell is represented as a vertical fuel-centered boiling flow channel. The core neutronics are described by the point kinetics equations with one delayed neutron precursor group. The reactivity in the point kinetics equation depends upon the spatially averaged, time-dependent void fraction and the spatially averaged, time-dependent fuel temperature; hence, it couples the core neutronics with the thermal-hydraulics. An ODE for the boiling boundary is obtained by

spatially integrating the single-phase energy equation from the channel inlet to the boiling boundary by introducing a spatially linear but time-dependent temperature profile (equivalent to the spatially linear single-phase enthalpy profile used by Clause and Lahey (1991)). The homogeneous equilibrium model, in which no-slip flow and thermal equilibrium between the two-phases is assumed, is used to represent the two-phase thermal-hydraulics in the boiling channel. This heated channel model has been shown to lead to conservative results with respect to DWO instabilities (Rizwan-uddin and Dorning, 1986). The void propagation equation in the two-phase region is rewritten in terms of the quality by using the homogeneous equilibrium model relationship between the void fraction and the two-phase quality. This equation is then reduced to an ODE for the slope of the quality by introducing a spatially linear but time-dependent two-phase quality profile (equivalent to the spatially linear two-phase enthalpy profile used by Clause and Lahey (1991)). Pressure drops in the single-phase and two-phase regions are calculated by integrating the momentum equations for the respective regions. An ODE for the inlet velocity is obtained by equating the sum of the pressure drops in the single-phase region, in the two-phase region and those due to the channel inlet and the channel exit, to the externally imposed pressure drop. Assuming only radial conduction, the PDE for heat conduction in the fuel rod is reduced to a set of ODEs using two approaches—a standard eigenfunction expansion method is used in version 1 and in version 2 a variational method is used. Version 1 leads to a converging solution of the time-dependent heat conduction equation as the number of eigenfunctions retained in the expansion is increased. However, this approach is inefficient since a large number of eigenfunctions (hence, ODEs) is required in order to obtain a reasonably accurate solution. Version 2 on the other hand, yields results comparable to the converged solution for version 1 with far fewer ODEs, thereby keeping the number of ODEs required to represent the fuel rod dynamics small and retaining the simplicity of the overall BWR model.

The phase variables, which are dimensionless, are the neutron density $n(t)$, the average delayed neutron precursor concentration $c(t)$, the boiling boundary $\mu(t)$, the slope $s(t)$ of the spatially linear representation of the two-phase quality as a function of the distance above the boiling boundary, the inlet velocity $v(t)$ and finally, the fuel temperature coefficients in the single-phase region, $T_{i,1\phi}(t)$, and in the two-phase region, $T_{i,2\phi}(t)$. In version 1, $T_{i,1\phi}(t)$ and $T_{i,2\phi}(t)$ are the time-dependent coefficients in the eigenfunction expansions for the fuel temperature in the single- and two-phase regions, and in version 2, they are the time-dependent coefficients of the space-dependent functions in the space- and time-dependent trial function used in the variational method. The operating parameters are the control-rod-induced external reactivity ρ_{ext} , the inlet subcooling number N_{sub} and the external pressure drop ΔP_{ext} . The Roman and Greek symbols are defined in Appendix A and the details of the nondimensionalization of the variables and parameters are given in Appendix B.

The dynamical system that results from the model is of the form

$$\dot{X}(t) = F(X; \gamma, \kappa) \quad (1)$$

where $X(t)$ is the vector of phase variables

$$X(t) = (n(t), c(t), \mu(t), s(t), v(t), T_{i,1\phi}(t), T_{i,2\phi}(t))^T, \quad (2)$$

γ is the vector of system operating parameters

$$\gamma = (\rho_{\text{ext}}, N_{\text{sub}}, \Delta P_{\text{ext}})^T, \quad (3)$$

and κ , the vector of design parameters

$$\kappa = (\text{Bi}, \text{Fr}, G_g, N_{f1}, N_{f2}, N_{\text{pch}}, N_r, N_{\text{sbo}}, N_\rho, T_{\text{sat}}, c_1, c_2, c_q, k_{\text{exit}}, k_{\text{inlet}}, r_1, A, \alpha_s, \beta, \lambda)^T \quad (4)$$

is suppressed throughout the rest of the paper for brevity.

More explicitly, the dimensionless system of ODEs that forms this dynamical system is

$$\frac{dn(t)}{dt} = \frac{\rho(t) - \beta}{A} n(t) + \lambda c(t) \quad (5)$$

$$\frac{dc(t)}{dt} = \frac{\beta}{A} n(t) - \lambda c(t) \quad (6)$$

$$\begin{aligned} \frac{d\mu(t)}{dt} &= 2v(t) - 2\mu(t) \\ &\times \frac{N_{\text{pch},1\phi}}{N_{\text{sub}}} [T_{s,1\phi}(t) - T_{\text{sat}} + N_{\text{sub}} N_{\text{sbo}}] \\ &\equiv f_1(t) \end{aligned} \quad (7)$$

$$\frac{ds(t)}{dt} = \frac{g_1(t) + s(t)f_1(t)}{g_2(t)} \quad (8)$$

$$\frac{dv(t)}{dt} = \frac{g_3(t) + g_4(t) + g_5(t)f_1(t)}{g_6(t)} \quad (9)$$

For version 1, the ODEs that represent the fuel rod dynamics are

$$\begin{aligned} \frac{dT_{i,j\phi}(t)}{dt} &= -\frac{\omega_{i,j\phi}^2 \alpha_s}{r_1^2} T_{i,j\phi}(t) \\ &+ \frac{2\alpha_s c_q \text{Bi}_{j\phi}}{(\omega_{i,j\phi}^2 + \text{Bi}_{j\phi}^2) J_0(\omega_{i,j\phi})} \Delta n(t), \\ &i = 1, 2, \dots, N \\ &j = 1, 2 \end{aligned} \quad (10)$$

and for version 2 they are

$$\begin{aligned} \frac{dT_{i,j\phi}(t)}{dt} &= l_{1,i,j\phi} T_{1,j\phi}(t) + l_{2,i,j\phi} T_{2,j\phi}(t) \\ &+ l_{3,i,j\phi} \Delta n(t), \quad i = 1, 2 \\ &j = 1, 2 \end{aligned} \quad (11)$$

In Eq. (5), $\rho(t)$ is the reactivity given by

$$\rho(t) = \rho_{\text{ext}} + c_1 \Delta \alpha(t) + c_2 \Delta T_{\text{avg}}(t) \quad (12)$$

where the external reactivity ρ_{ext} is the reactivity that results from the displacement of the control rods from their positions during normal operation of a reference BWR at 100% power. $\alpha(t)$ is the void fraction spatially averaged over the two-phase region and $T_{\text{avg}}(t)$ is the fuel temperature averaged over the rod cross-sectional area and the rod length (both the part in the single-phase region and the part in the two-phase region). Both $\Delta \alpha(t)$ and $\Delta T_{\text{avg}}(t)$ are then the changes measured from α_0 and $T_{\text{avg},0}$, their respective steady-state values at normal operation of a reference BWR at 100% power. In Eq. (7), $N_{\text{pch},1\phi}$ is the phase change number in the single-phase defined in terms of a reference temperature T_0^* , taken here

as T_{sat}^* . The temperature $T_{s,1\phi}(t)$ in that equation is the surface temperature of the fuel rod in the single-phase region and N_{sbo} is a dimensionless number given in Appendix B. The quantities $g_1(t), \dots, g_6(t)$ in Eqs. (8) and (9) are defined in the next section in the equations that arise in the development of the model. The index j in Eqs. (10) and (11) is one for the single-phase region and two for the two-phase region and $\Delta n(t) = n(t) - \tilde{n}$, where \tilde{n} is the steady-state (fixed point) value of the neutron density at a given set of system operating parameters γ . The quantities $r_1, \omega_{ij\phi}, \alpha_s, c_q, \text{Bi}_{j\phi}$, and J_0 in Eq. (10) are the fuel rod radius, the eigenvalues of the fuel-rod heat-conduction equation, the thermal diffusivity of the fuel, the ratio of the volumetric heat generation rate in the fuel rod to the average BWR core neutron density, the Biot number in phase j and the Bessel function of the first kind of order 0, respectively. The number of ODEs in Eq. (10), N , corresponds to the number of terms retained in the eigenfunction expansion for the fuel temperature in the two axial regions. In Eq. (11), $l_{1,i,j\phi}, l_{2,i,j\phi}$ and $l_{3,i,j\phi}$ are the constants that result when the heat conduction equation is integrated after substituting the trial function used in the variational method.

3. Development of the model

The point kinetics equations, Eqs. (5) and (6) in the dynamical system above, are well known, and a description of the remaining ODEs follows.

3.1. Equation (7)

Eq. (7) is obtained from the single-phase energy equation

$$\begin{aligned} \rho_f^* c_f^* \frac{\partial T^*(z^*, t^*)}{\partial t^*} + \rho_f^* c_f^* v^*(t^*) \frac{\partial T^*(z^*, t^*)}{\partial z^*} \\ = \frac{q''_{1\phi}(t^*) \xi^*}{A^*} \end{aligned} \quad (13)$$

where $q''_{1\phi}(t^*) = h_{1\phi}^* [T_{s,1\phi}^*(t^*) - (T_{\text{sat}}^* + T_{\text{inlet}}^*)/2]$ is the wall heat flux in the single-phase region. A spatially linear but time-dependent temperature profile $T_{1\phi}^*(z^*, t^*) = T_{\text{inlet}}^* + (T_{\text{sat}}^* - T_{\text{inlet}}^*)z^*/$

$\mu^*(t^*)$ is introduced (this is equivalent to that assumed for the single-phase enthalpy by Clause and Lahey (1991)) and the above equation is reduced to Eq. (7) by integrating from the inlet $z^* = 0$ to the boiling boundary $z^* = \mu^*(t^*)$.

3.2. Equation (8)

Eq. (8) is developed from the mixture-density equation which in dimensionless form is (Rizwan-uddin and Dorning, 1986)

$$\begin{aligned} \frac{\partial \rho_m(z, t)}{\partial t} + v_m(z, t) \frac{\partial \rho_m(z, t)}{\partial z} \\ = -N_{\text{pch},2\phi}(t) \rho_m(z, t), \end{aligned} \quad (14)$$

where $\rho_m(z, t)$ is the mixture-density and $v_m(z, t)$ is the mixture velocity given by (Rizwan-uddin and Dorning, 1986)

$$v_m(z, t) = v(t) + N_{\text{pch},2\phi}(t)[z - \mu(t)]. \quad (15)$$

Here the time-dependent dimensionless phase change number in the two-phase region is given by $N_{\text{pch},2\phi}(t) = \Gamma_g(t)/N_r$, where $\Gamma_g(t)$ is the vapor generation rate proportional to $q''_{2\phi}(t^*)$ —the wall heat flux in the two-phase region, here given by the Jens-Lottes correlation (for e.g. see Todreas and Kazimi (1990)). The vapor generation rate rewritten in terms of this correlation in SI units is

$$\Gamma_g(t) = G_g (T_{s,2\phi}(t) - T_{\text{sat}})^4 \quad (16)$$

where G_g is a dimensionless number that depends on the system pressure p_f^* and $T_{s,2\phi}(t)$ is the fuel rod surface temperature in the two-phase region. A spatially linear but time-dependent quality profile $x(z, t) = s(t)[z - \mu(t)]$ is introduced. This is equivalent to that assumed for the enthalpy by Clause and Lahey (1991) and leads to the following expression for the mixture density.

$$\rho_m(z, t) = \frac{1}{1 + s(t)[z - \mu(t)]/(N_\rho N_r)} \quad (17)$$

Eq. (17) is substituted into Eq. (14) for the mixture density which then is integrated from $z = \mu(t)$ to 1 to reduce it to Eq. (8), an ODE for the slope $s(t)$ of the spatially linear quality. The quantities $g_1(t)$ and $g_2(t)$ in Eq. (8) are given by

$$g_1(t) = \Gamma_g(t) N_\rho - v(t) s(t) \quad (18)$$

$$g_2(t) = \{1 + [1 - \mu(t)]s(t)/(N_\rho N_r)\} \times \frac{\log\{1 + [1 - \mu(t)]s(t)/(N_\rho N_r)\}}{[1 - \mu(t)]s^2(t)/(N_\rho N_r)^2} - \frac{1}{s(t)/(N_\rho N_r)} \quad (19)$$

3.3. Equation (9)

The dimensionless single-phase and two-phase momentum equations (Rizwan-uddin and Dorn-ing, 1986)

$$-\frac{\partial p_{1\phi}}{\partial z} = \frac{dv(t)}{dt} + N_{f1}v^2(t) + Fr^{-1} \quad (20)$$

$$-\frac{\partial p_{2\phi}}{\partial z} = \rho_m(z, t) \times \left[\frac{\partial v_m(z, t)}{\partial t} + v_m(z, t) \frac{\partial v_m(z, t)}{\partial z} + N_{f2}v_m^2(z, t) + Fr^{-1} \right] \quad (21)$$

are used to obtain Eq. (9), the ODE for the inlet velocity $v(t)$. The single-phase momentum equation Eq. (20), is integrated from $z = 0$ to $\mu(t)$ to give the single-phase region pressure drop and the two-phase momentum equation Eq. (21), is integrated from $z = (t)$ to 1 to obtain the two-phase region pressure drop. These pressure drops are summed along with the inlet and exit form pressure drops, and then equated to the external pressure drop ΔP_{ext} to arrive at Eq. (9). The functions $g_3(t)$, $g_4(t)$, $g_5(t)$ and $g_6(t)$ that appear in Eq. (9) are given by

$$g_3(t) = \Delta P_{\text{ext}} - \Delta P_{\text{inlet}}(t) - \Delta P_{\text{exit}}(t) - \Delta P_{\text{fric},1\phi}(t) - \Delta P_{\text{grav},1\phi}(t) - \Delta P_{\text{acc},2\phi}(t) - \Delta P_{\text{fric},2\phi}(t) - \Delta P_{\text{grav},2\phi}(t) \quad (22)$$

where explicit expressions for the seven internal channel pressure drops are given in Appendix C,

$$g_4(t) = -\frac{M_2(t)}{N_r} 4G_g(T_{s,2\phi}(t) - T_{\text{sat}})^3 g_7(t) \quad (23)$$

$$g_5(t) = \frac{1}{N_r} \Gamma_g(t) Q_1(t) \quad (24)$$

and

$$g_6(t) = \mu(t) + Q_1(t) \quad (25)$$

where $M_2(t)$ and $Q_1(t)$ are defined in Appendix C. The expression for $g_7(t)$ —which is equivalent to the time derivative of the two-phase region fuel surface temperature—is quite long and complex. Its detailed derivation is given below after the heat conduction equation is introduced and the fuel rod surface temperature in the two-phase region, $T_{s,2\phi}(t)$, is defined.

3.4. Equations (10) and (11)

Eqs. (10) and (11) are developed from the heat conduction equation for the fuel rod which in this simple model is taken as a single region, i.e. both the clad and the gap between the pin and the clad are omitted. That heat equation in cylindrical coordinates with conduction in the radial direction only, and with a time-dependent spatially-uniform volumetric heat generation rate $q'''(t^*)$ (which is directly proportional to the neutron density, $q'''(t^*) = c_q n^*(t^*)$)

$$\frac{\rho^* c_p^*}{k_d^*} \frac{\partial T_{j\phi}^*(r^*, t^*)}{\partial t^*} = \frac{\partial^2 T_{j\phi}^*(r^*, t^*)}{\partial r^{*2}} + \frac{1}{r^*} \frac{\partial T_{j\phi}^*(r^*, t^*)}{\partial r^*} + \frac{q'''(t^*)}{k_d^*}, \quad j = 1, 2 \quad (26)$$

must be solved with boundary conditions

$$|T_{j\phi}^*(0, t^*)| < \infty \text{ and} \\ -k_d^* \frac{\partial T_{j\phi}^*(r_1^*, t^*)}{\partial r^*} = h_{j\phi}^* (T_{j\phi}^*(r_1^*, t^*) - T_{b,j\phi}^*), \quad j = 1, 2 \quad (27)$$

where $T_{j\phi}^*(r^*, t^*)$ —the fuel rod temperature in the single-phase region for $j = 1$ and in the two-phase region for $j = 2$ —are treated separately in the regions below and above the moving boiling boundary and the solutions are not required to be continuous at the interface between these two regions. The single-phase heat transfer coefficient $h_{1\phi}^*$ is estimated by the Dittus-Boelter correlation, and the two-phase heat transfer coefficient $h_{2\phi}^*$ is estimated using the Jens-Lottes correlation (e.g. see Todreas and Kazimi (1990)). In Eq. (27), $T_{b,1\phi}^* = (T_{\text{sat}}^* + T_{\text{inlet}}^*)/2$ and $T_{b,2\phi}^* = T_{\text{sat}}^*$ are the bulk fluid

temperatures in the single-phase region and the two-phase region, respectively.

Eq. (26) is made dimensionless by using the dimensionless quantities $T_{j\phi}$, α_s , c_q , r_1 and $\text{Bi}_{j\phi}$ given in Appendix B. The steady-state solution of the heat conduction equation $\tilde{T}_{j\phi}(r)$ subject to the boundary conditions Eq. (27) then is

$$\tilde{T}_{j\phi}(r) = c_q \tilde{n} \left(\frac{r_1^2}{2\text{Bi}_{j\phi}} + \frac{r_1^2 - r^2}{4} \right) + T_{b,j\phi}, \quad j = 1, 2 \quad (28)$$

where $T_{b,1\phi} = T_{\text{sat}} - N_{\text{sub}}N_{\text{sbo}}$ and $T_{b,2\phi} = T_{\text{sat}}$. Now, by introducing the variable

$$\theta_{j\phi}(r, t) = T_{j\phi}(r, t) - \tilde{T}_{j\phi}(r), \quad j = 1, 2 \quad (29)$$

the dimensionless heat conduction equation becomes

$$\frac{1}{\alpha_s} \frac{\partial \theta_{j\phi}(r, t)}{\partial t} = \frac{\partial^2 \theta_{j\phi}(r, t)}{\partial r^2} + \frac{1}{r} \frac{\partial \theta_{j\phi}(r, t)}{\partial r} + c_q \Delta n(t), \quad j = 1, 2 \quad (30)$$

with boundary conditions

$$\begin{aligned} \frac{\partial \theta_{j\phi}(0, t)}{\partial r} &= 0 \\ \frac{\partial \theta_{j\phi}(r_1, t)}{\partial r} &= -\frac{\text{Bi}_{j\phi}}{r_1} \theta_{j\phi}(r_1, t) \end{aligned}, \quad j = 1, 2 \quad (31)$$

Eq. (30) with the boundary conditions, Eq. (31), is solved using two approaches—version 1 is a standard eigenfunction expansion method that leads to Eq. (10) and version 2 is a variational method that leads to Eq. (11). For version 1, a standard eigenfunction expansion

$$\theta_{j\phi}(r, t) = \sum_{i=1}^N T_{i,j\phi}(t) J_0\left(\frac{\omega_{i,j\phi} r}{r_1}\right), \quad j = 1, 2 \quad (32)$$

is introduced where $\omega_{i,j\phi}$ are the eigenvalues given by the transcendental equation

$$\omega_{i,j\phi} J_1(\omega_{i,j\phi}) = \text{Bi}_{j\phi} J_0(\omega_{i,j\phi}), \quad i = 1, 2, \dots, N \quad j = 1, 2 \quad (33)$$

Substituting Eq. (32) into Eq. (30) and after using the orthogonality of the Bessel functions

$$\begin{aligned} &\int_0^{r_1} J_0\left(\frac{\omega_{i,j\phi} r}{r_1}\right) J_0\left(\frac{\omega_{k,j\phi} r}{r_1}\right) r \, dr \\ &= \frac{r_1^2}{2} J_1^2(\omega_{i,j\phi}) \left(1 + \frac{\omega_{i,j\phi}^2}{\text{Bi}_{j\phi}^2}\right), \quad i = k, \quad j = 1, 2 \\ &= 0, \quad i \neq k \end{aligned} \quad (34)$$

etc, we arrive at the ODEs for the time-dependent coefficients $T_{i,j\phi}(t)$ given by Eq. (10) above.

For version 2, Eq. (30) can be written as $H\theta = f$ where the operator $H = \nabla^2$ is in cylindrical coordinates and $f = 1/\alpha_s \partial \theta / \partial t - \Delta n(t)$. Here and throughout the application of the variational method, for simplicity of notation we have omitted the subscript $j\phi$ from all the terms with an understanding that the analysis is either for the single-phase region ($j = 1$), or for the two-phase region ($j = 2$). We introduce a general functional $\mathcal{F}(\varphi)$ that accommodates discontinuous trial functions $\varphi(r, t)$, that need not satisfy the boundary conditions (Eq. (31))

$$\begin{aligned} \mathcal{F}(\varphi) &= (\varphi, H\varphi) - 2(\varphi, f) \\ &+ \left[\frac{r_1^2}{2\text{Bi}} \left(\frac{\partial \varphi}{\partial r} \right)^2 - \frac{\text{Bi}}{2} \varphi^2 \right]_{r=r_1} \\ &- \left[\frac{r_1^2}{2} \left(\frac{\partial \varphi}{\partial r} \right)^2 \right]_{r=0} \\ &+ r_d \left[\varphi_1 \frac{\partial \varphi_r}{\partial r} - \varphi_r \frac{\partial \varphi_1}{\partial r} \right]_{r=r_d} \end{aligned} \quad (35)$$

where the notation (a, b) indicates the inner product of a and b given by

$$(a, b) = \int_0^{r_1} a(r)b(r)r \, dr, \quad (36)$$

r_d is the point of discontinuity, and the subscripts 1 and r stand for the value of the function at the left and right of the discontinuity, respectively. The function that minimizes this functional is the solution $\varphi = \theta$ that satisfies $H\theta = f$ subject to the boundary conditions (Eq. (31)). The procedure for constructing this functional can be found in Kantorovich and Krylov (1964) and Stackgold (1968), and is not elaborated here.

We follow the Rayleigh-Ritz procedure (Kantorovich and Krylov, 1964; Stackgold, 1968) to approximately minimize the functional in Eq. (35) and arrive at the ODEs in Eq. (11). To do this, we substitute a two-piecewise quadratic trial function

$$\begin{aligned} \theta(r, t) &= T_1(t)v_{1a}(r) + T_2(t)v_{1b}(r), & 0 < r < r_d \\ &= T_1(t)v_{2a}(r) + T_2(t)v_{2b}(r), & r_d < r < r_1 \end{aligned} \quad (37)$$

into the functional $\mathcal{F}(\varphi)$ and adjust $T_1(t)$ and $T_2(t)$ so as to minimize \mathcal{F} . This is accomplished by setting $\delta\mathcal{F}/\delta T_1 = 0$ and $\delta\mathcal{F}/\delta T_2 = 0$. The resulting two equations can be solved simultaneously to arrive at the ODEs in Eq. (11) above. The quadratic functions $v_{1a}(r)$, $v_{1b}(r)$, $v_{2a}(r)$ and $v_{2b}(r)$ used in the final calculations actually reported here are such that the trial function $\theta(r, t)$ satisfies the boundary conditions (Eq. (31)) and is continuous and smooth at r_d . The details of the derivation of these quadratic functions are given in Appendix D. The details that lead to the expressions for $l_{1,i,j\phi}$, $l_{2,i,j\phi}$ and $l_{3,i,j\phi}$ in Eq. (11) are given in Appendix E.

3.5. Equation (12)

Though Eq. (12) is trivial, it involves $\Delta\alpha(t) (\equiv \alpha(t) - \alpha_0)$ and $\Delta T_{\text{avg}}(t) (\equiv T_{\text{avg}}(t) - T_{\text{avg},0})$ which must be expressed in terms of the other phase variables. The average void fraction in the channel $\alpha(t)$ is

$$\begin{aligned} \alpha(t) &= \frac{1}{[1 - \mu(t)]} \int_{\mu(t)}^1 \alpha(z, t) dz \\ &= \frac{1}{[1 - \mu(t)]} \int_{\mu(t)}^1 N_r \frac{x(z, t)}{N_\rho N_r + x(z, t)} dz \\ &= N_r \left\{ 1 - \frac{Q_1(t)}{[1 - \mu(t)]} \right\} \end{aligned} \quad (38)$$

and the average fuel temperature $T_{\text{avg}}(t)$ is given by

$$T_{\text{avg}}(t) = \mu(t)T_{\text{avg},1\phi}(t) + [1 - \mu(t)]T_{\text{avg},2\phi}(t) \quad (39)$$

where $T_{\text{avg},j\phi}(t)$ is given by Eq. (40) below.

This completes the formal development of the set of equations, Eqs. (5)–(12). To be able to carry out the stability analyses and numerical simulations, the intermediate variables, the average temperature in the fuel rod, $T_{\text{avg},j\phi}(t)$, the fuel rod surface temperature, $T_{s,j\phi}(t)$ and $g_7(t) (\equiv dT_{s,2\phi}(t)/dt)$ that arise in Eqs. (7), (16), (23) and (39) of the model, must be appropriately defined in terms of the phase variables $T_{i,j\phi}(t)$. In fact,

Eqs. (5)–(9) of the dynamical system are related to Eqs. (10) and (11) only through these intermediate variables. First, by multiplying each term in Eq. (29) with $2r/r_1^2$ and then integrating that equation from 0 to r_1 gives $T_{\text{avg},j\phi}(t)$ as

$$T_{\text{avg},j\phi}(t) = \theta_{\text{avg},j\phi}(t) + \tilde{T}_{\text{avg},j\phi}, \quad j = 1, 2$$

$$T_{\text{avg},j\phi}(t) = \frac{2}{r_1^2} \int_0^{r_1} T_{j\phi}(r, t) r dr,$$

and

$$\theta_{\text{avg},j\phi}(t) = \frac{2}{r_1^2} \int_0^{r_1} \theta_{j\phi}(r, t) r dr \quad (40)$$

where the $T_{i,j\phi}(t)$ dependence in the above equation enters through $\theta_{j\phi}(r, t)$, taken from Eq. (32) for version 1 and Eq. (37) for version 2. The steady-state average temperature, $\tilde{T}_{\text{avg},j\phi}$, in the above equation is obtained from Eq. (28)

$$\begin{aligned} \tilde{T}_{\text{avg},j\phi} &= \frac{2}{r_1^2} \int_0^{r_1} \tilde{T}_{j\phi}(r) r dr \\ &= c_q \tilde{n} r_1^2 \left(\frac{1}{2\text{Bi}_{j\phi}} + \frac{1}{8} \right) + T_{b,j\phi}, \quad j = 1, 2 \end{aligned} \quad (41)$$

Now, evaluating Eq. (29) at r_1 gives $T_{s,j\phi}(t)$ as

$$T_{s,j\phi}(t) = T_{j\phi}(r_1, t) = \theta_{s,j\phi}(t) + \tilde{T}_{s,j\phi}, \quad j = 1, 2 \quad (42)$$

where the steady-state surface temperature, $\tilde{T}_{s,j\phi} = \tilde{T}_{j\phi}(r_1)$ is obtained from Eq. (28). The surface temperature $\theta_{s,j\phi}(t) = \theta_{j\phi}(r_1, t)$ can be defined in two ways—either directly from Eqs. (32) and (37), or by relating it to the average quantity defined in Eq. (40). For example, $\theta_{s,j\phi}(t)$ obtained for version 1 by using Eq. (32) can be written as

$$\theta_{s,j\phi}(t) = \theta_{j\phi}(r_1, t) = \sum_{i=1}^N T_{i,j\phi}(t) J_0(\omega_{i,j\phi}) \quad j = 1, 2 \quad (43)$$

and for version 2 by using Eq. (37)

$$\theta_{s,j\phi}(t) = T_1(t)v_{2a}(r_1) + T_2(t)v_{2b}(r_1) \quad (44)$$

where the subscript $j\phi$ has been omitted from the terms on the right side of the equation. For both versions, version 1 and 2, $\theta_{s,j\phi}(t)$ can also be defined by relating it to the average quantity defined in Eq. (40). This relationship is obtained by multiplying each term in Eq. (30) with $2r/r_1^2$

and then integrating that equation from 0 to r_1 , which yields

$$\theta_{s,j\phi}(t) = \frac{r_1^2}{2\text{Bi}_{j\phi}} \left[c_q \Delta n(t) - \frac{1}{\alpha_s} \frac{d\theta_{\text{avg},j\phi}(t)}{dt} \right],$$

$$j = 1, 2 \quad (45)$$

Based on these two definitions for $\theta_{s,j\phi}(t)$, we subdivide version 1 (based on the eigenfunction expansion approach) into two subdivisions: version 1a based on Eq. (43) and version 1b based on Eq. (45). Eq. (44) for version 2, which is equivalent to Eq. (43) for version 1, is however not used because, as explained in the next paragraph, Eq. (45) yielded better results than Eq. (43) for version 1. Hence, we do not subdivide version 2, and only use the definition of $\theta_{s,j\phi}(t)$ given by Eq. (45) for the variational approach. Finally, expressions for the term $g_7(t) (\equiv dT_{s,2\phi}(t)/dt)$ in Eq. (23) now can be straightforwardly derived from Eqs. (43) and (45) for versions 1a and 1b, respectively and from Eq. (45) for version 2. These expressions are algebraically very complicated, and hence not given here explicitly.

In the next section we shall compare the stability boundaries in the $N_{\text{sub}}-\rho_{\text{ext}}$ operating parameter plane that result from versions 1a and 1b and version 2, for a fixed ΔP_{ext} —the pressure drop at normal operation of a reference BWR at 100% power. We shall show that for version 1a, the convergence of the stability boundary in the operating parameter plane with respect to N —the number of ODEs retained in Eq. (10) of the dynamical system—is very slow. For version 1b on the other hand, the convergence is much faster, indicating that version 1b can accurately represent the fuel rod dynamics with fewer ODEs, and hence, is better and simpler than version 1a. Further, we shall show that version 2 is comprised of the least number of ODEs by far, and accurately represents the fuel rod dynamics, thereby making it the simplest of the three models developed here.

Although version 2 is by far the simplest model, it became so only after the most suitable or the ‘best’ trial function given by Eq. (37), was determined—and determining such a function is a major disadvantage of the variational method. Before selecting the function in Eq. (37) as the most suitable trial function, various other trial

functions were tried and in each case, the resulting stability boundary in the $N_{\text{sub}}-\rho_{\text{ext}}$ operating parameter plane for a fixed ΔP_{ext} was compared to a reference stability boundary—taken here as the one from version 1b with $N = 32$. First, trial functions with one time-dependent coefficient were tried. The spatial dependence of the trial function in this category was a constant that did not satisfy the boundary conditions and a quadratic function that did satisfy the boundary conditions. However, in both these cases, the resulting stability boundary agreed rather poorly with the reference stability boundary. The next step was to try trial functions with two time-dependent coefficients. In this category, two-piecewise constants were tried which also did not do well. Finally, a two-piecewise quadratic trial function (Eq. (37)) that satisfied the boundary conditions and was continuous and smooth at r_d was tried. The resulting stability boundary agreed well with the reference stability boundary. For this case, the respective sizes of the two sub-divisions as determined by $r_d (0 < r_d < r_1)$, must be decided a priori. For this purpose, stability boundaries were determined for several values of the ratio r_d/r_1 and ΔP_{ext} and compared with reference stability boundaries. For ΔP_{ext} values of practical interest, it was determined that the ratio $r_d/r_1 = 0.83$ was best. This value subsequently was used in all the calculations reported here.

4. Stability analyses and numerical simulations

Stability analyses and numerical simulations were carried out using the simple dynamical system $\dot{\mathbf{X}}(t) = \mathbf{F}(\mathbf{X}; \gamma)$, developed in the previous section and given by Eqs. (5)–(11). The stability analyses were done using two approaches. In the first approach, the stability boundary in an operating parameter plane was generated directly by perturbing the vector of phase variables \mathbf{X} about a fixed point $\tilde{\mathbf{X}}$ (where tilde indicates the steady-state) as $\mathbf{X}(t) = \tilde{\mathbf{X}}(\gamma) + \delta \mathbf{X} e^{i\omega t}$ and then linearizing the dynamical system, which is then reduced to a set of two transcendental equations that involve the phase variables at the fixed point, the design and operating parameters and the oscilla-

tion frequency ω . The entire stability boundary in an operating parameter plane was generated by varying ω and solving these two equations directly for the two operating parameters. This approach, of course, corresponds to the case in which a complex conjugate pair of eigenvalues of the Jacobian matrix $F_X(\tilde{X}(\gamma); \gamma)$ evaluated at the fixed point $\tilde{X}(\gamma)$ have a zero real part and imaginary parts $\pm i\omega$ and suggests that a Hopf bifurcation occurs when the stability boundary in the parameter plane is crossed. In the second approach, the eigenvalues of the Jacobian matrix $F_X(\tilde{X}(\gamma); \gamma)$ at the fixed point $\tilde{X}(\gamma)$ were calculated. Any eigenvalue with a positive real part indicates that the corresponding fixed point is unstable and when—with all the other eigenvalues in the left half of the complex plane—a complex conjugate pair crosses the imaginary axis as a parameter is varied, a Hopf bifurcation is signaled. The special case in which the parameter values are such that the complex conjugate pair is on the imaginary axis, corresponds to the direct calculation (first approach) of the stability boundary. Finally, simulations were carried out by numerically integrating the full nonlinear ODEs in time. The results obtained via the direct calculation of the stability boundary, the calculation of the eigenvalues of the Jacobian matrix for various parameter values, and the full numerical simulations based on the time-dependent nonlinear ODEs are mutually consistent.

Typical design parameters and thermal-hydraulics data for operating conditions of a BWR (Todreas and Kazimi, 1990) and the neutronics data for the point kinetics equations (March-Leuba et al., 1986a,b; Duderstadt and Hamilton, 1976) are given in Appendix F. All the data are for the conditions at normal operation of a reference BWR at 100% power. Data for some design parameters such as k_{inlet} and k_{exit} had to be adjusted to lump the spacer pressure losses in the channel at the inlet and the exit.

Version 1 is represented by Eqs. (5)–(10) and it is further subdivided into two alternatives, versions 1a and 1b, based on the expressions used for the fuel rod surface temperature. For version 1a the fuel rod surface temperature is given by Eq. (43) and for version 1b it is given by Eq. (45).

Version 2 is represented by Eqs. (5)–(9) and (11) and is not further subdivided; the fuel rod surface temperature is given by Eq. (45) only. Fig. 1a shows the stability boundaries obtained using model versions 1a and 1b for various values of N plotted in the $N_{sub}-\rho_{ext}$ parameter plane for a fixed ΔP_{ext} —the core pressure drop at normal operation of a reference BWR at 100% power. As N is increased from 4 to 64, the stability boundaries for version 1a converge from left to right in the parameter plane and those for version 1b converge from right to left. Moreover, for

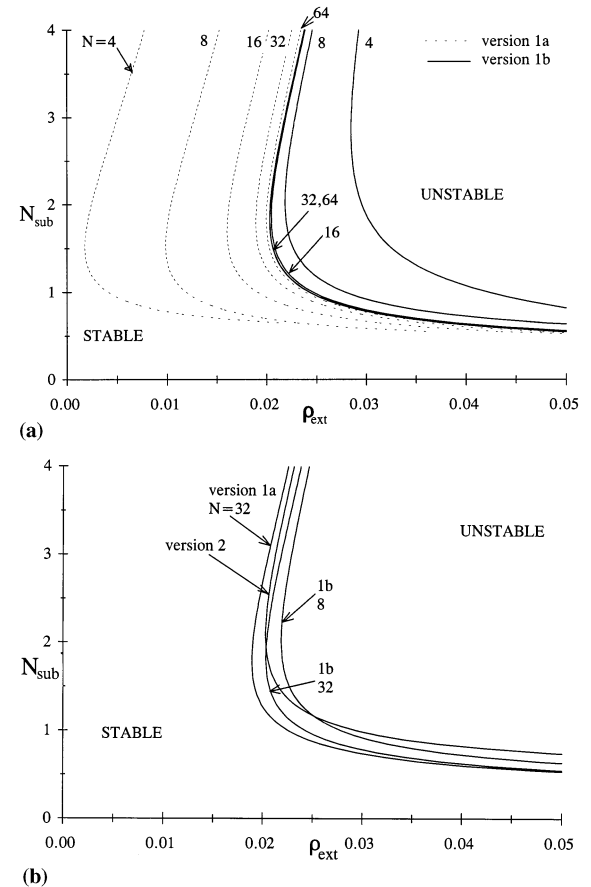


Fig. 1. (a) Sensitivity of the stability boundaries for model versions 1a and 1b in the $N_{sub}-\rho_{ext}$ parameter plane ($\Delta P_{ext} = 33.88$)— N —the number of terms in the eigenfunction expansion of the fuel rod temperature. (b) Comparison of the stability boundary in the $N_{sub}-\rho_{ext}$ parameter plane ($\Delta P_{ext} = 33.88$) of model version 2 with those for model version 1a for $N = 32$ and model version 1b for $N = 8$ and 32.

increasing N , the stability boundaries for versions 1a and 1b do not cross each other, but tend to converge to a single limit from opposite sides. This indicates that version 1a gives a lower bound and 1b gives an upper bound on the stability boundary. Further, for version 1b there is no perceptible shift in the stability boundary as N is increased above 32, indicating that the solution has reasonably well converged for $N = 32$. However, this is not so for version 1a—even when N is increased from 32 to 64. Hence, version 1b (in which the surface temperature was expressed in terms of the average temperature) is simpler than version 1a (in which the surface temperature was determined directly from the explicit expression for the temperature), since N is smaller for it, thereby resulting in a lower dimensionality of the dynamical system that is given by $(2N + 5)$. We take the stability boundary for version 1b for $N = 32$ as a reference stability boundary and compare the results for version 2 with it in Fig. 1b. It is clear from this figure that the stability boundary for version 2 with just two ODEs representing the fuel rod dynamics in each phase region agrees well with the reference stability boundary over most of the parameter plane and it lies within a lower bound given by version 1a for $N = 32$. Furthermore, considering that the stability boundary given by version 2 with only nine equations in the dynamical system is comparable in accuracy to the stability boundary given by version 1b for $N = 8$ that has a total of 21 equations, shows that the variational method approach is a reasonable compromise between retaining the simplicity of the model and the accuracy of the results. Hence, in the remainder of this paper, we carry out the stability analyses and numerical simulations using only version 2 of the model.

The stability boundary for version 2 replotted in the $N_{\text{sub}}-\rho_{\text{ext}}$ parameter plane for a fixed ΔP_{ext} ($= 33.88$) was calculated directly using the first approach described above, and is shown in Fig. 2. This boundary divides the operating parameter plane into the stable region, where the fixed point underline $\tilde{X}(\gamma)$ of the dynamical system at each $\gamma = (N_{\text{sub}}, \rho_{\text{ext}}, \Delta P_{\text{ext}})$ is stable and the unstable region where the fixed point is unstable. The

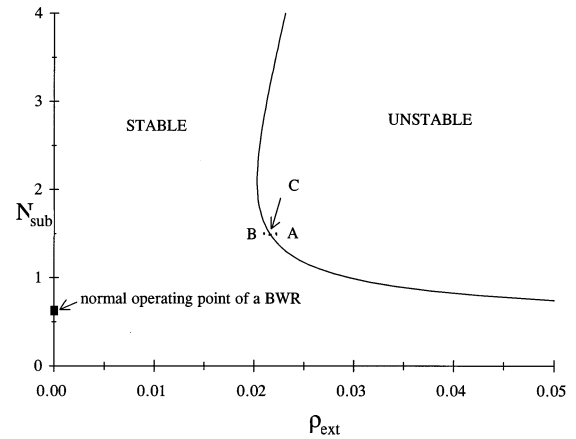


Fig. 2. The stability boundary of model version 2 in the $N_{\text{sub}}-\rho_{\text{ext}}$ parameter plane ($\Delta P_{\text{ext}} = 33.88$).

normal operating point of a BWR, for which $\rho_{\text{ext}} = 0$, $N_{\text{sub}} = 0.66$ and $\Delta P_{\text{ext}} = 33.88$, also is shown in Fig. 2. Clearly, this point lies well within the stable region in the operating parameter plane. It is interesting to note that—above a certain critical $\rho_{\text{ext}}^c = 0.02096$ —while increasing N_{sub} from an initially small value (for fixed ρ_{ext}) makes the system unstable, further increasing it eventually leads to a stable system again. As expected, for a fixed N_{sub} , increasing ρ_{ext} (which corresponds physically to moving the control rods out of the core) leads the system from a stable to an unstable state.

The results of the direct calculation of the stability boundary summarized above were checked by calculating the eigenvalues of the Jacobian matrix evaluated at the fixed point for various points in the $N_{\text{sub}}-\rho_{\text{ext}}$ parameter plane. The need to check the results of the direct calculation arises because, though there is a pair of complex conjugate eigenvalues with zero real part for parameter values on the stability boundary, there is no guarantee that there are no eigenvalues with positive real part for these parameter values. Moreover, it is also necessary to ensure that the complex conjugate pair of eigenvalues cross the imaginary axis as the parameters are varied, since this is a necessary condition for Hopf bifurcation. The computed eigenvalues yielded the same stable and unstable regions. For example, all the eigen-

values at the point A in the unstable region of Fig. 2—where the parameter values $(N_{\text{sub}}, \rho_{\text{ext}}) = (1.50, 0.02258)$ (and $\Delta P_{\text{ext}} = 33.88$) and the phase variables at the corresponding fixed point $(\tilde{n}, \tilde{c}, \tilde{\mu}, \tilde{s}, \tilde{v}) = (1.69, 2950, 0.23, 0.35, 0.88)$ —there is a complex conjugate pair with positive real part and all the other eigenvalues have negative real parts; and for the parameter values at the point B in the stable region of Fig. 2—where $(N_{\text{sub}}, \rho_{\text{ext}}) = (1.50, 0.02058)$ (and $\Delta P_{\text{ext}} = 33.88$) and the phase variables at the corresponding fixed point $(\tilde{n}, \tilde{c}, \tilde{\mu}, \tilde{s}, \tilde{v}) = (1.64, 2863, 0.25, 0.33, 0.90)$ —all the eigenvalues have negative real parts. Hence, the steady-state or fixed point is unstable for the parameter values corresponding to point A in the $N_{\text{sub}}-\rho_{\text{ext}}$ parameter plane and stable for those corresponding to point B. At the point C—where $(N_{\text{sub}}, \rho_{\text{ext}}) = (1.50, 0.02158)$ —which lies on the stability boundary in Fig. 2, there is a complex conjugate pair with zero real part and non-zero imaginary part $\pm i\omega$ with $\omega = 13.48$ (or, $\omega^* = 1.5$ Hz); all the other eigenvalues have negative real parts. Points A and B in Fig. 2 are very close to point C. Hence, as the parameter ρ_{ext} is decreased through its value on the stability boundary, a complex conjugate pair of eigenvalues of $F_X(\tilde{X}(\gamma), \gamma)$ crosses the imaginary axis indicating that the system does indeed undergo a Hopf bifurcation (Hale and Kocak, 1991; Hassard et al., 1981). The fixed point is completely specified only by the fixed point values of all the phase variables, i.e. $\tilde{X}(\gamma) = (\tilde{n}, \tilde{c}, \mu, \tilde{s}, \tilde{v}, \tilde{T}_{1,1\phi}, \tilde{T}_{2,1\phi}, \tilde{T}_{1,2\phi}, \tilde{T}_{2,2\phi})$. However, only the first five are given above, because $\tilde{T}_{i,j\phi}$ $i = 1, 2$ $j = 1, 2$ are always zero at a fixed point (because in Eq. (11), $\Delta n = 0$, and in general, $l_{1,1,j\phi} l_{2,2,j\phi} \neq l_{2,1,j\phi} l_{1,2,j\phi}$ at the fixed point) and therefore, we have not indicated them in the fixed point.

Finally, numerical simulations were carried out for several points in the operating parameter plane to study the nonlinear effects not captured by the local bifurcation and stability analyses. For initial conditions only ‘slightly’ away from the fixed points, the results of the numerical simulations always agreed with those of the stability analyses, i.e. growing oscillations resulted for points on the unstable side of the stability

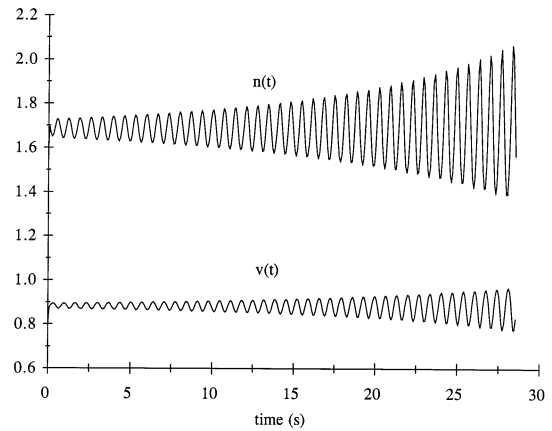


Fig. 3. Time evolution of phase variables for parameter values at point A in Fig. 2. Initial condition, $(n(0), c(0), \mu(0), s(0), v(0)) = (1.60, 2950, 0.23, 0.35, 0.80)$ and all $T(0)$'s = 0, is nearby the unstable fixed point $(\tilde{n}, \tilde{c}, \tilde{\mu}, \tilde{s}, \tilde{v}) = (1.69, 2950, 0.23, 0.35, 0.88)$.

boundary in the parameter plane and decaying oscillations (back to the fixed point) resulted for points on the stable side. Shown in Figs. 3–6 are the results of the numerical simulations carried out at point A (in the unstable region) and at point B (in the stable region) in Fig. 2. The time evolution of the neutron density $n(t)$ and the inlet

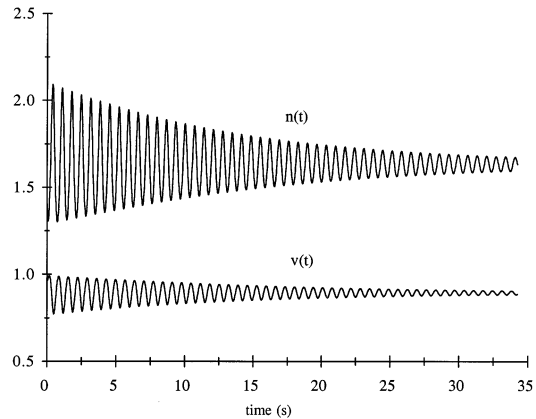


Fig. 4. Time evolution of phase variables for parameter values at point B in Fig. 2. Initial condition, $(n(0), c(0), \mu(0), s(0), v(0)) = (2.50, 2863, 0.23, 0.33, 1.00)$ and all $T(0)$'s = 0, is nearby the stable fixed point $(\tilde{n}, \tilde{c}, \tilde{\mu}, \tilde{s}, \tilde{v}) = (1.64, 2863, 0.25, 0.33, 0.90)$.

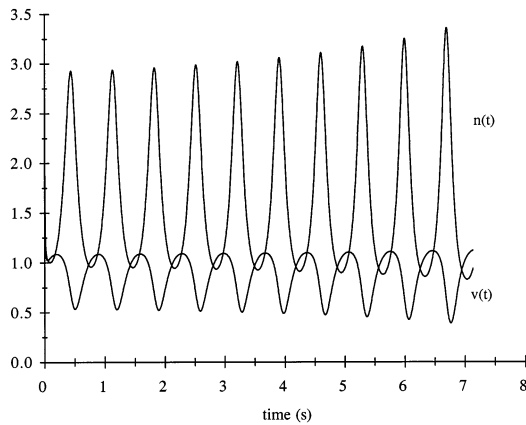


Fig. 5. Time evolution of phase variables for parameter values at point B in Fig. 2. Initial condition, $(n(0), c(0), \mu(0), s(0), v(0)) = (3.00, 2863, 0.20, 0.33, 1.10)$ and all $T(0)$'s = 0, is some distance away from the stable fixed point $(\bar{n}, \bar{c}, \bar{\mu}, \bar{s}, \bar{v}) = (1.64, 2863, 0.25, 0.33, 0.90)$.

velocity $v(t)$, when the system parameters are at point A, starting from initial condition $(n(0), c(0), \mu(0), s(0), v(0)) = (1.60, 2950, 0.23, 0.35, 0.80)$ and $T_{i,j\phi}(0) = 0, i = 1, 2; j = 1, 2$ nearby the fixed point, is shown in Fig. 3. As expected on the basis of the stability analyses, the oscillation amplitudes grow and the system moves away from the unstable fixed point. The time evolution of $n(t)$ and

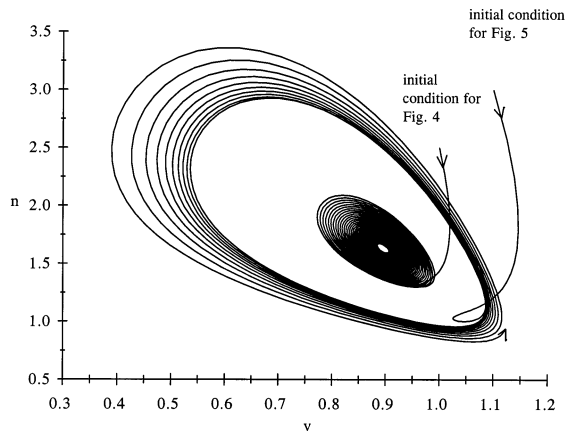


Fig. 6. Phase portrait. Evolution of the phase space trajectories in the projection of the phase space onto the $n-v$ plane for parameter values at point B in Fig. 2 for two different sets of initial conditions.

$v(t)$ for parameter values at point B, starting from initial condition $(n(0), c(0), \mu(0), s(0), v(0)) = (2.50, 2863, 0.23, 0.33, 1.00)$ and all $T(0)$'s = 0 close to the fixed point, is shown in Fig. 4. Also as expected from the stability results, the oscillations decay in this case and the system evolves to the stable fixed point. However, when the initial condition for the numerical simulation is taken farther away from the fixed point corresponding to point B in Fig. 2, i.e. $(n(0), c(0), \mu(0), s(0), v(0)) = (3.00, 2863, 0.20, 0.33, 1.10)$ and all $T(0)$'s = 0, the system moves away from the fixed point. The time evolution of the neutron density and the inlet velocity for this case is shown in Fig. 5, where the oscillation amplitude of the phase variables now grows in time. The time evolutions of $n(t)$ and $v(t)$ in Figs. 4 and 5 are plotted in Fig. 6 as phase-portraits projected onto the $n-v$ phase plane. The trajectory that emanates from the initial conditions used in Fig. 4, moves towards the stable fixed point, whereas the one that emanates from the initial conditions used in Fig. 5, evolves away from the fixed point. These two phase portraits, shown in Fig. 6, indicate that there exists an unstable limit cycle in the phase space nearby the stable fixed point when the parameter values are at point B and thus that the Hopf bifurcation that occurs as the stability boundary in Fig. 2 is crossed is a subcritical Hopf bifurcation, not a supercritical Hopf bifurcation. This is consistent with the fact that the growing oscillations, that result from the simulation done for parameter values at point A, do not saturate at a stable limit cycle which would indicate that the Hopf bifurcation is supercritical. Hence, when the system is operated at the allegedly 'safe' parameter values corresponding to point B, for which the fixed point is stable, an initial condition that could result due to a finite perturbation from that fixed point would lead to growing oscillations, not oscillations that would die away and evolve to the fixed point. Thus, although the steady-state or the fixed point corresponding to the point B in Fig. 2 is stable, it may not be a safe point at which to operate the BWR since a small but finite perturbation could lead to growing nuclear-coupled

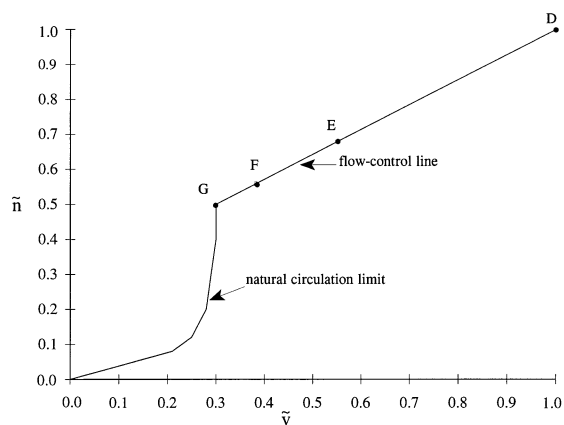


Fig. 7. A typical power-flow map for a BWR (Wulff et al., 1992).

density-wave oscillations as indeed the simulation (Figs. 5 and 6) shows. This, of course, typically is the case when a subcritical Hopf bifurcation occurs. These results are consistent with the results reported by Tsuji et al. (1993) who also showed in the stability analysis of their model that a subcritical Hopf bifurcation occurred as the stability boundary was crossed.

The frequencies of oscillations obtained from the numerical simulations were compared with those evaluated via the eigenvalue calculations. The points A and B in Fig. 2 are very close to the point C which is on the stability boundary. Hence, the damped and growing oscillations, that occur for parameter values at A and B, respectively, following initial conditions very close to the corresponding fixed point values, should have frequencies very close to the imaginary part of the eigenvalues—the complex conjugate pair that has zero real part—of the Jacobian matrix for parameter values at point C. Indeed, the growing and damped neutron densities and inlet velocities shown in Figs. 3 and 4 for parameter values at points A and B respectively, oscillate with frequency 1.5 Hz, consistent with the eigenvalues of the Jacobian matrix corresponding to the point C.

The stability results just described can be related to the operating regimes on the power-flow map familiar to BWR plant engineers. A typical power-flow map for a BWR (Wulff et al., 1992) is

shown in Fig. 7. This power-flow map also can be referred to as an \tilde{n} – \tilde{v} map (as in Fig. 7) since the power can be related directly to the steady-state (fixed point) neutron density \tilde{n} and the flow rate can be related directly to the steady-state inlet velocity \tilde{v} . The map is generated from the natural circulation limit and the forced-convection flow-control line of a BWR. For most operational transients, flow-control is used to follow BWR load changes. This method of load-following ensures that the system pressure is essentially constant and reduces the need for control rod action on the flow-control line. Point D on this line in Fig. 7 is the normal operating point of a BWR, points E and F correspond to operating conditions with 20 and 30 K subcooling, respectively and point G is known to correspond to the least stable BWR operating conditions (March-Leuba et al., 1986a,b). This line D–G is the flow-control line used to follow load changes.

Keeping in mind both that the model developed and analyzed here is a very simple BWR core model and that not all design and operating parameters are available for an actual BWR, we do not attempt a detailed quantitative comparison with all possible operating points on the power-flow map. Rather, we use the results of the stability analyses and numerical simulations described above to explain qualitatively the change in stability between the normal BWR operating point, point D, and the least stable operating point, point G, in the power-flow map shown in Fig. 7. The flow-control line, D–G in Fig. 7 is mapped to the $N_{\text{sub}}-\tilde{n}$ operating-parameter/phase-variable plane in Fig. 8. Unlike previous stability boundaries generated directly in an operating parameter plane by keeping the third operating parameter fixed, the stability boundary for a fixed inlet velocity was first generated in the $N_{\text{sub}}-\rho_{\text{ext}}$ parameter plane by keeping the steady-state inlet velocity \tilde{v} fixed and allowing the third operating parameter ΔP_{ext} to vary. This stability boundary was then mapped to the $N_{\text{sub}}-\tilde{n}$ plane and is shown in Fig. 8. Since operating points D, E, F and G have different fixed-point inlet velocities— $\tilde{v} = 1.0, 0.55, 0.39$ and 0.3 , respectively—there are correspondingly different stability boundaries for them. The operating point D in Fig. 8 is related to

the $\tilde{v} = 1.0$ stability boundary, and clearly lies well within the stable region defined by that boundary. The operating point E in Fig. 8 is related to the $\tilde{v} = 0.55$ stability boundary and we observe that point E is closer to that boundary than point D is to the $\tilde{v} = 1.0$ stability boundary. Hence, although the point E is stable, it is less stable than D in the sense that it would be more easily susceptible to diverging oscillations when the initial conditions are not near the fixed point. Such diverging oscillations for a fixed point on the stable side of the stability boundary were indeed demonstrated for the point B in Fig. 2. The decreasing stability of the operating points continues as they are moved down the flow-control line to point F which is related to the $\tilde{v} = 0.39$ stability boundary, and finally to point G which is related to the $\tilde{v} = 0.3$ stability boundary. Point G is the closest point to its stability boundary; hence, it is clear that among all the operating points on the flow-control line, point G is the least stable operating point and point D is the most stable since it is farthest from its stability boundary. We reiterate here that this explanation is very qualitative, limited not only by the simplicity of the model, but also by the unavailability of accurate data for design and operating parameters. For example, the stability boundaries that were shown to be

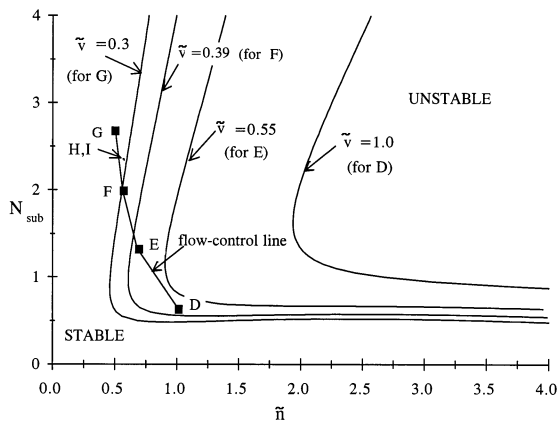


Fig. 8. Stability boundaries in the $N_{\text{sub}}-\tilde{n}$ operating-parameter/phase-variable plane for four fixed values of the inlet velocity—each value corresponds to a point on the flow-control line (points D, E, F and G in Fig. 7). Points H and I are essentially indistinguishable on the scale used here.

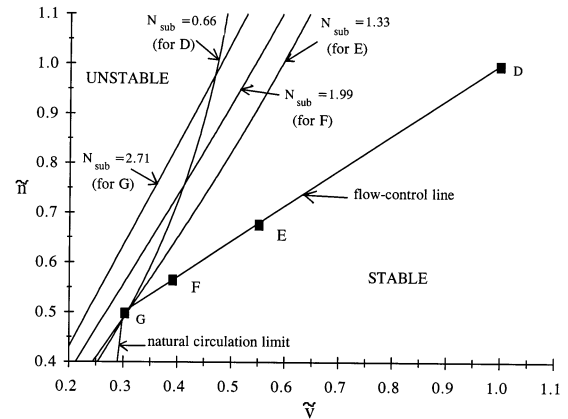


Fig. 9. Stability boundaries in the $\tilde{n}-\tilde{v}$ phase-variable plane for four fixed values of the inlet subcooling—each value corresponds to a point on the flow-control line.

sensitive to design parameters such as the pressure loss coefficients, friction factors, feedback coefficients, etc. by Tsuji et al. (1993), shift appreciably when these parameters are varied. Depending on the values of these parameters, according to our calculations the point G could be on the unstable side of the stability boundary for $\tilde{v} = 0.3$ which corresponds to it, clearly making it an unstable operating point; or, the point G could be a little further into the stable region of the $N_{\text{sub}}-\tilde{n}$ plane. In either case, the overall trend of decreasing stability of operating points on the flow-control line as the flow rate is reduced, will continue to be exhibited in Fig. 8 and that is what we have attempted to establish here as quantitatively as possible in the absence of proprietary design data (and a complicated detailed engineering model).

The decreasing stability of the operating points on the flow-control line as the flow rate is reduced, can also be observed from Fig. 9, where the stability boundaries are plotted for four fixed values of $N_{\text{sub}} = 0.66, 1.33, 1.99$ and 2.71 , corresponding to the inlet subcooling at points D, E, F and G, respectively in Fig. 7. These stability boundaries were first generated directly in the $\Delta P_{\text{ext}}-\rho_{\text{ext}}$ operating parameter plane by keeping the third operating parameter, N_{sub} , fixed. They then were mapped on to the $\tilde{n}-\tilde{v}$ plane and are shown in Fig. 9. Operating point D can now be

related to the $N_{\text{sub}} = 0.66$ stability boundary and we observe that it is very stable. Points E, F and G can be related to their respective stability boundaries and we observe that the corresponding stability boundaries move closer to the operating points as we move along the flow-control line from E to F and finally to G. This again demonstrates the decreasing stability of the operating points as we move down the flow-control line. It is interesting to observe that the stability boundary for fixed N_{sub} in this plane passes through a minimum as N_{sub} is increased from its value at the point D—the stability boundary moves to the right as N_{sub} is increased from 0.66 to 1.33 and then starts moving back to the left as N_{sub} is increased further to 2.71.

One of the possible consequences of subcritical Hopf bifurcation was illustrated in Figs. 4–6, which showed that for the same set of operating parameters values that correspond to a stable fixed point, transients initiating from two different initial conditions may lead either to oscillations decaying to the stable fixed point, or more importantly, to oscillations with growing amplitude diverging away from the stable fixed point. From a BWR operations perspective, another important consequence of the subcritical Hopf bifurcation is that by changing the operating parameters from a point in the stable region to two operating points that are nearby each other and closer to the stability boundary—but both in the stable region—may lead to oscillations that converge to the stable fixed point in one case and to oscillations that diverge from the second nearby stable fixed point in the other. As an illustration, Fig. 10 shows the time evolution of the neutron density $n(t)$ initiated from the phase variables corresponding to the fixed point values at point G (with a 20% reduction in the initial boiling boundary, $\mu(0)$, that was necessary to prevent the inlet velocity from becoming negative during the initial transient oscillations rendering the model developed and used here irrelevant), as operating parameters are changed at $t = 0$ to a point H in Fig. 8 defined by the new set of operating parameters, $(\rho_{\text{ext}}, N_{\text{sub}}, \Delta P_{\text{ext}}) = (0.011011, 2.205, 6.4421)$. Clearly, the transient is converging to the stable fixed point corresponding to point H given by

$N_{\text{sub}} = 2.205$ and $(\tilde{n}, \tilde{v}) = (0.55388, 0.3)$. Also shown in Fig. 10 is the time evolution of the neutron density $n(t)$ initiated from the same initial conditions as before, i.e. from point G (with a 20% reduction in the initial boiling boundary, $\mu(0)$), as operating parameters at $t = 0$ are changed to a point I in the parameter space defined by $(\rho_{\text{ext}}, N_{\text{sub}}, \Delta P_{\text{ext}}) = (0.011011, 2.2, 6.4407)$, that also is in the stable region very close to the point H. The oscillations in this case diverge from the the new stable fixed point corresponding to point I, given by $N_{\text{sub}} = 2.2$ and $(\tilde{n}, \tilde{v}) = (0.55346, 0.3)$. The converging and diverging transients which start from the same initial conditions and result from a change from the same operating point to two operating points very close to each other (both in the stable region), also are shown as phase plane trajectories in Fig. 11, in which the phase portraits projected onto the $n-v$ phase plane are shown for parameter values corresponding to the points H and I.

5. Summary and conclusions

A simple model, that led to a representation of a BWR core as a low-dimensional dynamical system comprised of a set of nonlinear ODEs, has

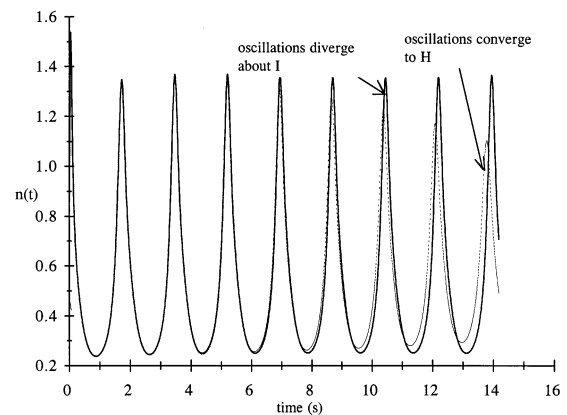


Fig. 10. The converging oscillations (to the fixed point corresponding to point H in Fig. 8) and the diverging oscillations (about the fixed point corresponding to point I in Fig. 8) of $n(t)$ that are initiated by changing the operating parameters from point G to points H and I in Fig. 8.

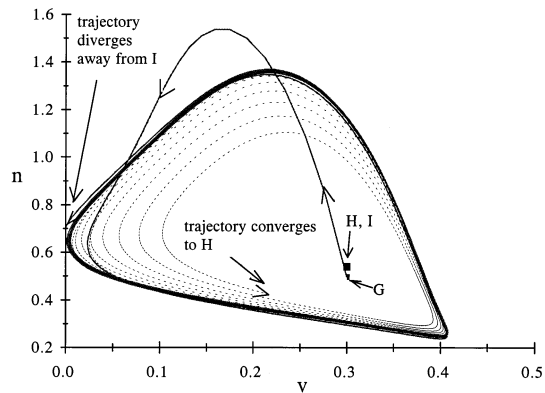


Fig. 11. Phase portrait. Evolution of the phase space trajectories in the projection of the phase space onto the n - v plane for parameter values at point H (converging to the corresponding fixed point) and for those at point I (diverging from the corresponding fixed point) for the same initial condition—the fixed point corresponding to the point G in Fig. 8.

been developed for stability analyses and transient simulations. A BWR (fuel) lattice cell was represented as a vertical fuel-centered boiling flow channel. The neutronics was modeled by the point kinetics equations with one precursor group and the two-phase region thermal-hydraulics in the channel was represented by the homogeneous equilibrium model. The equations for the single-phase temperature and the two-phase quality were reduced to ODEs by approximating these quantities by spatially linear but time-dependent functions in a weighted-residual-like approach with weighing functions of unity. Finally, the PDE for heat conduction in the fuel rod was reduced to a set of ODEs using two approaches—version 1 was based on an eigenfunction expansion method and version 2 was based on a variational method. These two approaches were compared in terms of stability boundaries plotted in the $N_{\text{sub}}-\rho_{\text{ext}}$ operating parameter plane for a fixed ΔP_{ext} . Based on conflicting objectives of improving the stability boundary accuracy and reducing the number of equations in the dynamical system, the variational method was determined to be the best choice; therefore, only the dynamical system with the heat conduction PDE reduced to a set

of ODEs via the variational method, was used for the main stability analyses and numerical simulations.

The stability boundary was calculated directly and plotted in the $N_{\text{sub}}-\rho_{\text{ext}}$ operating parameter plane for a fixed ΔP_{ext} . The eigenvalues of the Jacobian matrix of the dynamical system were computed at the fixed points corresponding to various points in that $N_{\text{sub}}-\rho_{\text{ext}}$ operating parameter plane. The results of these eigenvalue calculations were consistent with the stability analysis, and indicated that a Hopf bifurcation occurs as the stability boundary is crossed. Also, time-dependent numerical simulations of the nonlinear equations were carried out for points on both sides of this stability boundary, and the results were consistent with those of the stability analysis. Further numerical simulations with different initial conditions indicated that the Hopf bifurcation is subcritical, and that an unstable limit cycle exists along with the stable fixed point (steady-state) for parameter values in the stable region nearby the stability boundary. The practical implications thus could be important because when the system is operated on the allegedly ‘safe’ (stable) side of the stability boundary, but near it, notwithstanding the fact that the fixed point is stable, a finite perturbation from it could lead to DWOs with growing amplitudes—which indeed occurred for the simple model studied here. Although a subcritical Hopf bifurcation observed here supports the fact that no sustained oscillations were observed in stability tests at low-flow/high-power operating conditions performed at several operating plants (Ward and Lee, 1987), we may also conclude that the stable limit cycle oscillations observed at other operating plants (Ward and Lee, 1987) are not excited directly by this subcritical Hopf bifurcation.

Finally, the flow-control line was mapped to $N_{\text{sub}}-\tilde{n}$ operating-parameter/phase-variable plane. The decreasing stability of the operating points on the flow-control line as the flow rate is reduced was shown by comparing the mapped curve with stability boundaries plotted for four fixed inlet velocities in that operating-parameter/

phase-variable plane. Stability boundaries also were plotted in the $\tilde{n}-\tilde{v}$ phase variable plane for four fixed inlet subcooling numbers corresponding to four operating points on the flow-control line and the decreasing stability of the operating points on the flow-control line as the flow rate is reduced was then shown by relating those points to their respective stability boundaries. Thus operating points on the power-flow map were related to the stability boundaries in an operating-parameter/phase-variable plane and in a phase variable plane and a qualitative explanation was given for the instabilities observed at the least stable operating point on the flow-control line of the power-flow map. It was also shown that the normal operating point of a BWR at 100% power is very stable in comparison with other operating points on the power flow map.

Appendix A. Nomenclature

A	cross sectional flow area
Bi	Biot number
D_h	diameter = $4 A/\xi$
Fr	Froude number
J_0	Bessel function of first kind order 0
J_1	Bessel function of first kind order 1
L	channel length
N	number of ODEs in Eq. (10)
N_f	friction number
N_{pch}	phase change number
N_{sub}	subcooling number
P	pressure
T	temperature
c	precursor concentration
c_1	void reactivity coefficient
c_2	fuel temperature coefficient
c_f	liquid specific heat
c_q	$q'''^*(t^*) \equiv c_q^* n^*(t^*)$
f	friction factor
g	gravitational constant
h	heat transfer coefficient
h_f	liquid enthalpy
h_g	vapor enthalpy
k_d	fuel conductivity
k_{exit}	exit pressure loss coefficient

k_f	liquid conductivity
k_{inlet}	inlet pressure loss coefficient
n	neutron density
p	system pressure
q''	wall heat flux
q'''	volumetric heat generation rate
r_1	fuel rod radius
s	quality slope
v	velocity
x	quality
Γ_g	vapor generation rate
Δh_{fg}	enthalpy difference, $h_g - h_f$
Δn	neutron density difference, $n - \tilde{n}$
$\Delta \rho$	density difference, $\rho_f - \rho_g$
Λ	delayed neutron generation time
α	void fraction
α_s	thermal diffusivity = $k_d/(\rho c_p)_{fuel}$
β	delayed neutron fraction
θ	temperature difference, $T - \tilde{T}$
λ	precursor decay constant
μ	boiling boundary
μ_f	liquid viscosity
ξ	heated perimeter
ρ	reactivity
ρ_f	liquid density
ρ_g	vapor density
ω	frequency
$\omega_{i,j\phi}$	eigenvalues

Subscripts

1ϕ	single-phase
2ϕ	two-phase
avg	average
b	bulk
ext	external
f	liquid
g	vapor
l	left
m	mixture
0	reference
r	right
s	surface
sat	saturation

Superscripts

\sim	steady-state (fixed point)
*	dimensional quantity

Appendix B

The dimensionless variables and parameters used in the BWR model are listed below. The asterisks indicate the original dimensional quantities.

$$\begin{aligned}
 \text{Bi}_{j\phi} &= \frac{h_{j\phi}^* r_1^*}{k_d^*}, \quad j = 1, 2 & \text{Fr} &= \frac{v_0^{*2}}{g^* L^*} & G_g &= \frac{2.56e^{4p^*/6.2 \cdot 10^6} \zeta^* T_0^{*4} L^*}{\Delta h_{fg}^* A^* v_0^* \rho_g^*} \\
 N_{fj} &= \frac{f_{j\phi} L^*}{2D_h^*}, \quad j = 1, 2 & N_{\text{pch},1\phi} &= \frac{h_{1\phi}^* T_0^* \zeta^* L^* \Delta \rho^*}{A^* \Delta h_{fg}^* \rho_g^* \rho_f^* v_0^*} & N_r &= \frac{\rho_f^*}{\Delta \rho^*} \\
 N_{\text{sbo}} &= \frac{\Delta h_{fg}^* \rho_g^*}{2c_f^* T_0^* \Delta \rho^*} & N_{\text{sub}} &= \frac{c_f^* (T_{\text{sat}}^* - T_{\text{inlet}}^*) \Delta \rho^*}{\Delta h_{fg}^* \rho_g^*} & N_\rho &= \frac{\rho_g^*}{\rho_f^*} \\
 T_{i,j\phi} &= \frac{T_{i,j\phi}^*}{T_0^*}, \quad i = \text{s, avg, 1, 2} & T_{j\phi}(r, t) &= \frac{T_{j\phi}^*(r^*, t^*)}{T_0^*}, \quad j = 1, 2 & T_{\text{sat}} &= \frac{T_{\text{sat}}^*}{T_0^*} \\
 c &= \frac{c^*}{n_0^*} & c_2 &= c_2^* T_0^* \\
 c_q &= \frac{c_q^* L^* n_0^*}{k_d^* T_0^*} & n &= \frac{n^*}{n_0^*} & r_1 &= \frac{r_1^*}{L^*} \\
 s &= s^* L^* & t &= \frac{t^* v_0^*}{L^*} & v &= \frac{v^*}{v_0^*} \\
 \Gamma_g(t) &= \frac{q_{2\phi}^{*'}(t^*) \zeta^* L^*}{A^* \Delta h_{fg}^* v_0^* \rho_g^*} & \Delta P_{\text{ext}} &= \frac{\Delta P_{\text{ext}}^*}{\rho_f^* v_0^{*2}} & \Lambda &= \frac{\Lambda^* v_0^*}{L^*} \\
 \alpha_s &= \frac{\alpha_s^*}{v_0^* L^*} & \lambda &= \frac{\lambda^* L^*}{v_0^*} & \mu &= \frac{\mu^*}{L^*}
 \end{aligned}$$

Appendix C

The expressions for the seven internal pressure drops that appear in Eq. (22) are:

$$\Delta P_{\text{inlet}}(t) = k_{\text{inlet}} v^2(t) \quad (\text{C1})$$

$$\Delta P_{\text{exit}}(t) = k_{\text{exit}} \frac{1}{1 + [1 - \mu(t)][s(t)/(N_\rho N_r)]} \{v(t) + N_{\text{pch},2\phi} [1 - \mu(t)]\}^2 \quad (\text{C2})$$

$$\Delta P_{\text{fric},1\phi}(t) = N_{f1} v^2(t) \mu(t) \quad (\text{C3})$$

$$\Delta P_{\text{grav},1\phi}(t) = \frac{\mu(t)}{\text{Fr}} \quad (\text{C4})$$

$$\Delta P_{\text{acc},2\phi}(t) = N_{\text{pch},2\phi}(t) [v(t) Q_1(t) + N_{\text{pch},2\phi}(t) M_2(t)] \quad (\text{C5})$$

$$\Delta P_{\text{fric},2\phi}(t) = N_{f2} [v^2(t) Q_1(t) + 2N_{\text{pch},2\phi}(t) v(t) M_2(t) + N_{\text{pch},2\phi}^2(t) M_3(t)] \quad (\text{C6})$$

$$\Delta P_{\text{grav},2\phi}(t) = \frac{Q_1(t)}{\text{Fr}} \quad (\text{C7})$$

where $Q_1(t)$, $M_2(t)$ and $M_3(t)$ are defined as

$$Q_1(t) = \int_{\mu(t)}^1 \rho_m(z, t) dz = \frac{1}{s(t)/(N_\rho N_r)} \log \{1 + [1 - \mu(t)][s(t)/(N_\rho N_r)]\} \quad (\text{C8})$$

$$M_2(t) = \int_{\mu(t)}^1 \rho_m(z, t)[z - \mu(t)] dz$$

$$= \frac{1}{s(t)/(N_\rho N_r)} \{[1 - \mu(t)] - Q_1(t)\} \quad (C9)$$

$$M_3(t) = \frac{1}{s(t)/(N_\rho N_r)} \left[\frac{[1 - \mu(t)]^2}{2} - M_2(t) \right] \quad (C10)$$

and the subscripts fric, grav and acc indicate that these pressure drops are due respectively to friction, gravity and the acceleration associated with the convective term in the substantial derivative.

Appendix D

The most general form of the quadratic expressions for $v_{1a}(r)$, $v_{1b}(r)$, $v_{2a}(r)$ and $v_{2b}(r)$ in Eq. (37) can be simplified using the appropriate boundary conditions on domain boundaries and using continuity and smoothness (continuity of first derivatives) conditions at the interface between sub-domains. For simplicity of notation, the subscript $j\phi$ on all the terms indicating the phase is omitted with an understanding that the analysis is either for the single-phase region ($j = 1$), or the two-phase region ($j = 2$). The function $\theta(r, t)$ in Eq. (37) is written as a two-piecewise quadratic function

$$\theta(r, t) = T_1(t) + a_1(t)r + a_2(t)r^2, \quad 0 \leq r \leq r_d$$

$$= T_2(t) + b_1(t)r + b_2(t)r^2, \quad r_d \leq r \leq r_1 \quad (D1)$$

where T_1 , a_1 , a_2 , T_2 , b_1 and b_2 are the time-dependent coefficients. The function $\theta(r, t)$ in Eq. (D1) satisfies the following four conditions

$$\partial\theta(0, t)/\partial r = 0 \quad (D2)$$

$$\partial\theta(r_1, t)/\partial r = -(\text{Bi}/r_1)\theta(r_1, t) \quad (D3)$$

$$\theta_1(r_d, t) = \theta_r(r_d, t) \quad (D4)$$

$$\partial\theta_1(r_d, t)/\partial r = \partial\theta_r(r_d, t)/\partial r \quad (D5)$$

where Eqs. (D4) and (D5) are respectively, the continuity and smoothness conditions at $r = r_d$ and the subscripts l and r indicate the limits from the left and right, respectively. Application of Eq.

(D2) gives $a_1(t) = 0$. Using Eqs. (D3), (D4) and (D5), the quantities a_2 , b_1 , and b_2 in Eq. (D1) are eliminated in terms of T_1 and T_2 as:

$$a_2(t) = a_{2a}T_1(t) + a_{2b}T_2(t)$$

$$b_1(t) = b_{1a}T_1(t) + b_{1b}T_2(t) \quad (D6)$$

$$b_2(t) = b_{2a}T_1(t) + b_{2b}T_2(t)$$

where, a_{2a} , a_{2b} , b_{1a} , b_{1b} , b_{2a} and b_{2b} are constants. Substituting Eq. (D6) into Eq. (D1) and comparing it with Eq. (37) gives:

$$v_{1a}(r) = 1 + a_{2a}r^2$$

$$v_{1b}(r) = a_{2b}r^2 \quad (D7)$$

$$v_{2a}(r) = b_{1a}r + b_{2a}r^2$$

$$v_{2b}(r) = 1 + b_{1b}r + b_{2b}r^2$$

Explicit expressions for the constants a_{2a} , a_{2b} , b_{1a} , b_{1b} , b_{2a} and b_{2b} are algebraically very complicated; hence, they are not given here. Following the procedure described above, they can easily be obtained from symbolic manipulation packages such as Mathematica or Maple, as was carried out in the research reported here.

Appendix E

The detailed derivation of Eq. (11)—the ODEs for fuel rod dynamics for version 2 of the model, obtained using the variational method to solve the heat conduction equation—is presented below. For simplicity of notation, the subscript $j\phi$ on all the terms indicating the phase is omitted with an understanding that the analysis is either for the single-phase region ($j = 1$) or the two-phase region ($j = 2$).

Following the Rayleigh-Ritz procedure (Kantorovich and Krylov, 1964; Stackgold, 1968), the variations $\delta\mathcal{F}/\delta T_1$ and $\delta\mathcal{F}/\delta T_2$ for the functional in Eq. (35) are set equal to zero to obtain the following two ODEs (note that although f in Eq. (35) includes the term $\partial\theta/\partial t$, it is treated as a constant when taking the variations)

$$m_1 \frac{dT_1(t)}{dt} + m_2 \frac{dT_2(t)}{dt}$$

$$= m_3 T_1(t) + m_4 T_2(t) + m_5 c_q \Delta n(t)$$

$$\begin{aligned} & n_1 \frac{dT_1(t)}{dt} + n_2 \frac{dT_2(t)}{dt} \\ & = n_3 T_1(t) + n_4 T_2(t) + n_5 c_q \Delta n(t) \end{aligned} \quad (\text{E1})$$

where

$$\begin{aligned} m_1 &\equiv (v_{1aa} + v_{2aa})/\alpha_s, & m_2 &\equiv (v_{1ab} + v_{2ab})/\alpha_s, \\ m_3 &\equiv v_{1aHa} + v_{2aHa}, & m_4 &\equiv v_{1aHb} + v_{2aHb}, \\ m_5 &\equiv c_q \Delta n(t)(v_{1a1} + v_{2a1}), \\ n_1 &\equiv (v_{1ba} + v_{2ba})/\alpha_s, & n_2 &\equiv (v_{1bb} + v_{2bb})/\alpha_s, \\ n_3 &\equiv v_{1bHa} + v_{2bHa}, & n_4 &\equiv v_{1bHb} + v_{2bHb} \end{aligned}$$

and

$$n_5 \equiv c_q \Delta n(t)(v_{1b1} + v_{2b1}). \quad (\text{E2})$$

The shortened notations for the inner products used in the above equation are given by:

$$\begin{aligned} v_{1aHa} &= (v_{1a}, H v_{1a}), & v_{1aHb} &= (v_{1a}, H v_{1b}), \\ v_{2aHa} &= (v_{2a}, H v_{2a}), & v_{1aa} &= (v_{1a}, v_{1a}), \\ v_{2ab} &= (v_{2a}, v_{2b}), & v_{1a1} &= (v_{1a}, 1), \text{ etc.} \end{aligned} \quad (\text{E3})$$

where the first subscript indicates the domain of integration in the inner product; 1 for the inner sub-domain from 0 to r_d and 2 for the outer sub-domain from r_d to r_1 .

Eq. (E1) can be solved simultaneously to arrive at Eq. (11)—the ODEs for version 2—where

$$\begin{aligned} l_{1,i} &= (-m_k n_3 + n_k m_3)/\Delta \\ l_{2,i} &= (-m_k n_4 + n_k m_4)/\Delta \\ l_{3,i} &= (-m_k n_5 + n_k m_5)/\Delta \\ \Delta &= m_1 n_2 - n_1 m_2 \end{aligned} \quad (\text{E4})$$

with $k=2$ when $i=1$ and $k=1$ when $i=2$.

It should be noted that since the operator $H = \nabla^2$ is self-adjoint and the final trial function used here (Eq. (37)) satisfies the boundary conditions (Eq. (31)) and is smooth at r_d , the Rayleigh-Ritz method becomes identical to the Bubnov-Galerkin method (Kantorovich and Krylov, 1964; Stackgold, 1968).

Appendix F

In this paper, the following typical BWR design and operating parameters (March-Leuba et al., 1986a; Todreas and Kazimi, 1990; Duderstadt and Hamilton, 1976) were used:

$$\begin{aligned} A^* &= 1.442 \times 10^{-4} \text{ m}^2 & k_{\text{inlet}} &= 15 \\ L^* &= 3.81 \text{ m} & p^* &= 7.2 \times 10^6 \text{ N m}^{-2} \\ T_{\text{inlet}}^* &= 551 \text{ K} & r_1^* &= 6.135 \times 10^{-3} \text{ m} \\ T_0^* &= 561 \text{ K} & v_0^* &= 2.67 \text{ m s}^{-1} \\ T_{\text{sat}}^* &= 561 \text{ K} & \Delta h_{\text{fg}}^* &= 1494.2 \times 10^3 \text{ J kg}^{-1} \\ c_1 &= -0.15 & \Delta P_{\text{ext}}^* &= 177.88 \times 10^3 \text{ N m}^{-2} \\ c_2^* &= -2.0 \times 10^{-5} \text{ K}^{-1} & \Lambda^* &= 4.0 \times 10^{-5} \text{ s} \\ c_f^* &= 5.307 \times 10^3 \text{ J kg}^{-1} \text{ K}^{-1} & \alpha_s^* &= 1.398 \times 10^{-6} \text{ m}^2 \text{ s}^{-1} \\ c_q^* &= 3.148 \times 10^{-6} \text{ W m}^{-3} \text{ cm}^2 \text{ s} & \beta &= 0.0056 \\ f_{1\phi} &= 0.01467 & \lambda^* &= 0.08 \text{ s}^{-1} \\ f_{2\phi} &= 0.01467 & \mu_f^* &= 9.750 \times 10^{-5} \text{ N m}^{-2} \text{ s} \\ k_d^* &= 3.6 \text{ W m}^{-1} \text{ K}^{-1} & \zeta^* &= 3.855 \times 10^{-2} \text{ m} \\ k_{\text{exit}} &= 2.5 & \rho_f^* &= 736.49 \text{ kg m}^{-3} \\ k_f^* &= 5.740 \times 10^{-1} \text{ W m}^{-1} \text{ K}^{-1} & \rho_g^* &= 37.71 \text{ kg m}^{-3} \end{aligned}$$

References

- Achard, J.-L., Drew, D.A., Lahey, R., 1985. The analysis of nonlinear density-wave oscillations in boiling channels. *J. Fluid Mech.* 155, 213–232.
- Belblidia, L.A., Weaver, L.E., Carlson, R.W., 1983. Nodal analysis of density-wave oscillations in boiling water nuclear reactors. *Ann. Nucl. Energy* 10 (10), 505–534.
- Bergdahl, B.G., Reisch, F., Oguma, R., Lorenzen, J., Akerhielm, F., 1989. BWR stability investigation at Forsmark-1. *Ann. Nucl. Energy* 16 (10), 509–520.
- Clausse, A., Lahey, R.T., 1991. The analysis of periodic and strange attractors during density-wave oscillations in boiling flows. *Chaos Solitons Fractals* 1 (2), 167–178.
- Duderstadt, J.J., Hamilton, L.J., 1976. *Nuclear Reactor Analysis*. Wiley, New York.
- Hale, J.K., Kocak, H., 1991. *Dynamics and Bifurcations*. Springer-Verlag, New York.
- Hassard, B.D., Kazarinoff, N.D., Wan, Y.H., 1981. *Theory and Applications of Hopf Bifurcation*. Cambridge University Press, New York.
- Kantorovich, L.V., Krylov, V.I., 1964. *Approximate Methods of Higher Analysis*. Interscience, New York.
- March-Leuba, J., Cacuci, D.G., Perez, R.B., 1986a. Nonlinear dynamics and stability of boiling water reactors: Part I—Qualitative analysis. *Nucl. Sci. Eng.* 93, 111–123.
- March-Leuba, J., Cacuci, D.G., Perez, R.B., 1986b. Nonlinear dynamics and stability of boiling water reactors: Part II—Quantitative analysis. *Nucl. Sci. Eng.* 93, 124–136.
- Peng, S.J., Podowski, M.Z., Lahey, R.T., Becker, M., 1984. NUFREQ-NP: A computer code for the stability analysis of boiling water nuclear reactors. *Nucl. Sci. Eng.* 88, 404–411.
- Rizwan-uddin, Dorning, J.J., 1986. Some nonlinear dynamics of a heated channel. *Nucl. Eng. Des.* 93, 1–14.
- Rizwan-uddin, Dorning, J.J., 1992. Density-wave instabilities in advanced boiling water reactors. *ANS Proc. Natl. Heat Transfer Conf.* 6, 161–170.
- Stackgold, I., 1968. *Boundary Value Problems of Mathematical Physics—II*. Macmillan, New York.
- Todreas, N.E., Kazimi, M.S., 1990. *Nuclear Systems I—Thermal Hydraulics Fundamentals*. Hemisphere, New York.
- Tsuji, M., Nishio, K., Narita, M., 1993. Stability analysis of BWRs using bifurcation theory. *J. Nuc. Sci. Technol.* 30 (11), 1107–1119.
- Valtonen, K., 1989. *BWR stability analysis*. Finnish Center for Radiation and Nuclear Safety, Helsinki.
- Ward, M.E., Lee, J.C., 1987. Singular perturbation analysis of limit cycle behavior in nuclear-coupled density-wave oscillations. *Nucl. Sci. Eng.* 97, 190–202.
- Wulff, W., Cheng, H.S., Mallen, A.N., Rohatgi, U.S., 1992. BWR stability analysis with the BNL engineering plant analyzer. BNL-NUREG-52312.